6.1 Introduction

Chromium and tin substitution in $SrAl_4Fe_8O_{19}$ hexaferrite has been optimized in this chapter. Nonmagnetic Sn^{+4} ion has increased the M_s of SrM due to the replacement of Fe^{+3} ion from the opposite spin site, which is responsible for increasing the total magnetic moment. While, H_c is decreased because of the size of the grains and shape anisotropy [Fang *et al*. (2005)]. On the other side, if Fe^{+3} ions are substituted by magnetic ions, it changes the total magnetic moment depending upon the substituting sites available in the system. Jamalian (2015) have reported about Cr^{+3} doping, initially, M_s is increased but, later it is decreased with dopant concentration ($SrFe_{12-x}Cr_xO_{19}$ (x = 0-1)). Cr^{+3} has a tendency to replace Fe^{+3} at *12k, 2a* (spin up) and $4f_2$ (spin down) sites [Jamalian (2015)]. Therefore, if Cr^{+3} substitutes at spin up sites (*12k, 2a*), it decreases the net magnetic moment and if it is substituted at spin down sites ($4f_2$), it increases the total magnetic moment. Hence, it can be deduced that the magnetic properties of SrM can be manipulated with suitable substitutions as per necessity. Thus, it is important to study the doping effect of both magnetic and non-magnetic ions in SrM to engineer the materials with suitable magnetic properties.

In this work, an effort is made to investigate the combined effect of Cr^{+3} and Sn^{+4} at Fe^{+3} site in SrM. {$SrAl_4(Cr_{0.5}Sn_{0.5})_xFe_{8-x}O_{19}$ with x = 0.0, 0.2, 0.4, 0.6, & 0.8} ferrites have been synthesized by the sol-gel auto combustion method, as discussed in section 3.1.1. Rietveld refinement on X-ray Diffraction (XRD) patterns are performed to reveal the phase purity, crystal structure and unit cell parameters such as lattice constant, bond angles and bond lengths. The microstructure evolution, type of bonds, site occupancy, magnetic & dielectric properties of the ferrites have also been investigated.

6.2 Results and Discussion

FTIR spectroscopy is carried out in order to confirm the substitution preference of Cr^{+3} and Sn^{+4} among available Fe^{+3} sites and the presence of bonds [Luo *et al*. (2012), Ali *et al*. (2013)] in the structure. Figure 6.1 shows the FTIR graphs of the calcined $SrAl_4(Cr_{0.5}Sn_{0.5})_xFe_{8-x}O_{19}$ hexaferrite powders. As reported earlier, hexaferrite exhibits 189 optical modes, out of them only 31 (13 A_{2u} + 18 E_{1u}) are IR respond modes [Mahadevan *et al*. (2017)]. In the present case, only 3 are active modes 460, 568 and 628 cm^{-1}. Absorption bands between 400 to 800 cm^{-1} are the signature characteristic bands of $SrFe_{12}O_{19}$ [Baykal *et al.* (2012a), (2012b), Xie *et al.* (2012)]. The frequency around 460 cm^{-1} (υ_1) is ascribed to intrinsic stretching vibrations at the octahedral site of the metal cation [Gonzalez *et al*. (2017), Mahadevan *et al*. (2017)].

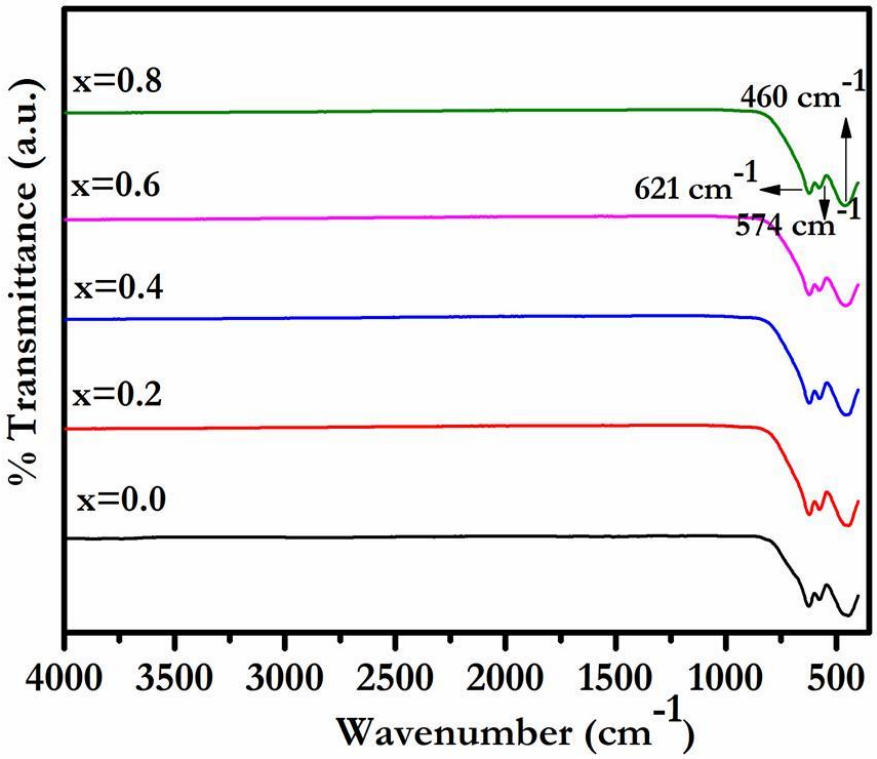

Figure 6.1 FTIR spectra of calcined $SrAl_4Fe_{(8-x)}(Cr_{0.5}Sn_{0.5})_xO_{19}$ ferrire powders.

On the other side, absorption frequencies around 568 cm^{-1} and 628 cm^{-1} (υ_2, υ_3) are due to stretching vibrations of the metal cation at the tetrahedral site [Gonzalez *et al*. (2017), Mahadevan *et al*. (2017)]. In Table 6.1, the vibrational intensities with the compositions are listed. It is noted from Table 6.1 that υ_1 varies while, υ_2, and υ_3 remain invariant with increasing Cr^{+3} and Sn^{+4} content. The shift in υ_1 towards higher intensity suggests that Fe^{+3} ion is being substituted by Cr^{+3} at the octahedral site. Eventually, Cr^{+3} has lesser atomic weight than the Fe^{+3} and the wave number is reciprocal to atomic weight [Mahadevan *et al*. (2017)]. For x = 0.8 composition, υ_1 shifts towards lower intensity, suggests that Fe^{+3} ion is being replaced by Sn^{+4} at the octahedral site due to higher atomic weight compare to Fe^{+3} ion. Higher the molecular weight, lower the vibration frequency and lower the wave numbers.

Table 6.1 Band position of $SrAl_4(Cr_{0.5}Sn_{0.5})_xFe_{8-x}O_{19}$ ferrites with ($0 \leq x \leq 0.8$).

Composition (x)	**υ_1 (cm^{-1})**	**υ_2 (cm^{-1})**	**υ_3 (cm^{-1})**
0.0	443.61	574.76	621.05
0.2	445.54	574.76	621.05
0.4	457.11	574.76	621.05
0.6	461.13	574.76	621.05
0.8	460.96	574.76	621.05

To identify the crystal structure features of $SrAl_4(Cr_{0.5}Sn_{0.5})_xFe_{8-x}O_{19}$ (x = 0.0, 0.2, 0.4, 0.6, & 0.8) ferrites, XRD is performed. Figure 6.2(a) depicts the XRD patterns of sintered ferrite samples which confirm the phase formation in all the compositions without any secondary or impurity phase. It is noted from the Figure 6.2(a) that the diffraction patterns are well harmonized with JCPDS No. 720739 standard of strontium hexaferrite with

P63/mmc space group [Debnath *et al*. (2015)]. Figure 6.2(b) shows the magnified view to show the XRD profiles shifting towards higher angle up to x = 0.6 later, it seems shifting towards the lower angle.

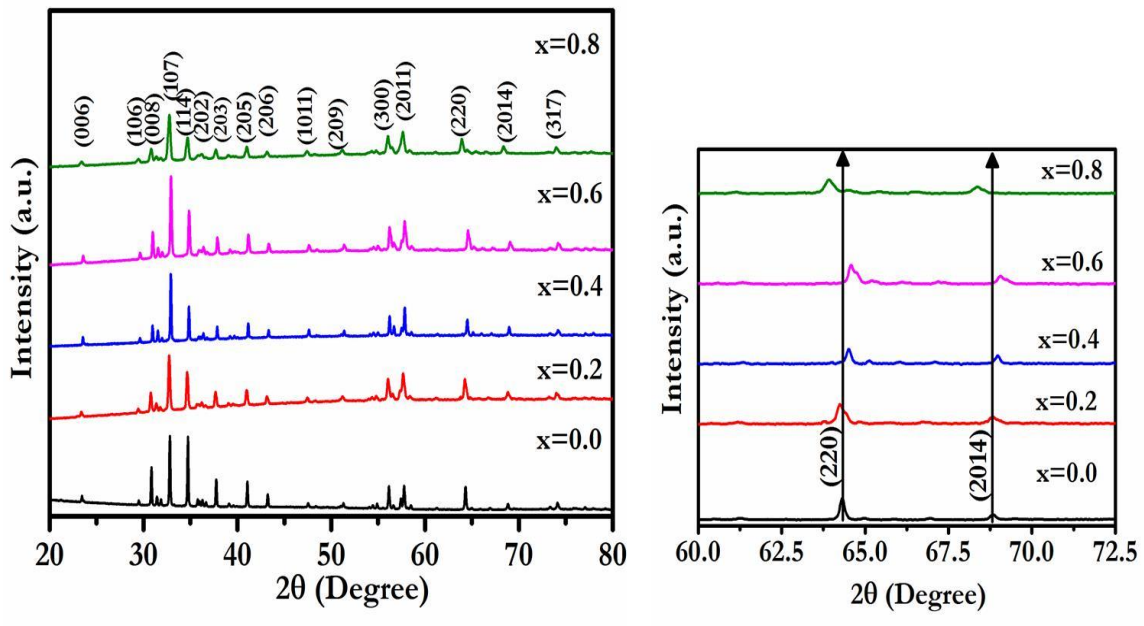

Figure 6.2 XRD pattern of sintered (a) $SrAl_4Fe_{(8-x)}(Cr_{0.5}Sn_{0.5})_xO_{19}$ ferrites, (b) XRD profiles shifting.

To further explore the structural parameters, Rietveld refinement is followed out by using the software FullProf with *P63/mmc* space group [Raju *et al*. (2018)]. Rietveld refinement of the XRD patterns of $SrAl_4Fe_8O_{19}$ and $SrAl_4(Cr_{0.5}Sn_{0.5})_{0.8}Fe_{7.2}O_{19}$ are manifested in Figure 6.3. During the refinement, scale-factor, zero-correction, lattice parameters, thermal parameters, asymmetry parameters, and atomic positions are refined simultaneously. Background and peak shapes are defined by the linear interpolation among set background points and pseudo-Voigt function, respectively. The credibility of the refinement is estimated by the low values of R_p, R_{wp} and goodness of fit (χ^2). The refined

parameters, i.e., reliable factors, lattice parameters, unit cell volume, *c/a* ratio, and crystallite size are included in Table 6.2 & Table 6.3.

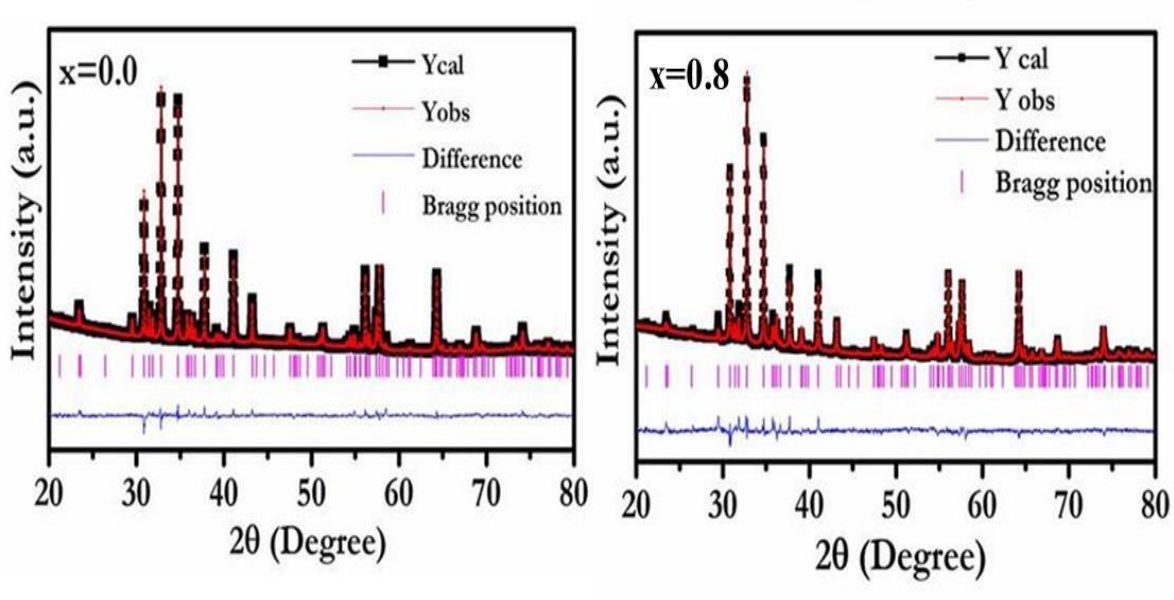

Figure 6.3 Rietveld refined pattern of sintered x = 0.0; $SrAl_4Fe_8O_{19}$ and x = 0.8; $SrAl_4Fe_{7.2}(Cr_{0.5}Sn_{0.5})_{0.8}O_{19}$ ferrites.

Table 6.2 R_p, R_{wp}, χ^2, lattice parameters, Volume, *c/a* ratio, crystallite size of $SrAl_4(Cr_{0.5}Sn_{0.5})_xFe_{8-x}O_{19}$ hexa-ferrites.

Composition (x)	**R_p (%)**	**R_{wp} (%)**	**χ^2**	**Lattice parameters** (Å)		**Volume (Å^3)**	***c/a***	**Crystallite size (nm)**
				(a)	***(c)***			
0	2.06	2.65	1.65	5.78	22.72	657.34	3.93	12.64
0.2	1.71	2.29	1.87	5.79	22.64	657.28	3.91	12.09
0.4	1.71	2.40	1.72	5.79	22.43	651.20	3.87	11.47
0.6	1.84	2.56	2.01	5.79	22.21	644.81	3.83	11.06
0.8	2.18	2.83	2.09	5.79	22.48	652.65	3.88	11.51

Table 6.3 Refined structural parameters of $SrAl_4(Cr_{0.5}Sn_{0.5})_xFe_{8-x}O_{19}$ hexaferrites.

Composition	Sites	x	y	z	Occ.
$SrFe_8Al_4O_{19}$	Sr (*2d*)	0.6667	0.3333	0.2500	1
	Fe1(*2a*)	0.0000	0.0000	0.0000	1
	Fe2(*2b*)	0.0000	0.0000	0.2531	1
	Fe3($4f_1$)	0.3333	0.6667	0.0282	2
	Fe4($4f_2$)	0.3333	0.6667	0.1900	2
	Fe5(*12k*)	0.1683	0.3366	-0.1083	2
	Al(*12k*)	0.1683	0.3366	-0.1083	4
	O 1(*4e*)	0.0000	0.0000	0.1480	2
	O2 (*4f*)	0.3333	0.6667	-0.0564	2
	O3 (*6h*)	0.1830	0.3650	0.2500	3
	O4 (*12k*)	0.1552	0.3101	0.0505	6
	O5 (*12k*)	0.5060	0.0110	0.1477	6
$Sr\ Al_4(Sn_{0.5}Cr_{0.5})_{0.2}Fe_{7.8}O_{19}$	Sr (*2d*)	0.6667	0.3333	0.2500	1
	Fe1(*2a*)	0.0000	0.0000	0.0000	1
	Fe2(*2b*)	0.0000	0.0000	0.2531	1
	Fe3($4f_1$)	0.3333	0.6667	0.0303	2
	Fe4($4f_2$)	0.3333	0.6667	0.1881	1.8
	Sn($4f_2$)	0.3333	0.6667	0.1881	0.1
	Cr($4f_2$)	0.3333	0.6667	0.1881	0.1
	Fe5(*12k*)	0.1699	0.3399	-0.1074	2
	Al(*12k*)	0.1699	0.3399	-0.1074	4
	O 1(*4e*)	0.0000	0.0000	0.1584	2
	O2 (*4f*)	0.3333	0.6667	-0.0619	2
	O3 (*6h*)	0.1510	0.3020	0.2500	3

	O4 (*12k*)	0.1390	0.2780	0.0517	6
	O5 (*12k*)	0.5020	0.0050	0.1436	6
$Sr\ Al_4(Sn_{0.5}Cr_{0.5})_{0.4}Fe_{7.6}O_{19}$	Sr (*2d*)	0.6667	0.3333	0.2500	1
	Fe1(*2a*)	0.0000	0.0000	0.0000	1
	Fe2(*2b*)	0.0000	0.0000	0.2531	1
	Fe3($4f_1$)	0.3333	0.6667	0.0288	2
	Fe4($4f_2$)	0.3333	0.6667	0.1872	1.6
	Sn($4f_2$)	0.3333	0.6667	0.1872	0.2
	Cr($4f_2$)	0.3333	0.6667	0.1872	0.2
	Fe5(*12k*)	0.1606	0.3214	-0.1076	2
	Al(*12k*)	0.1606	0.3214	-0.1076	4
	O 1(*4e*)	0.0000	0.0000	0.1954	2
	O2 (*4f*)	0.3333	0.6667	-0.0699	2
	O3 (*6h*)	0.1636	0.3271	0.2500	3
	O4 (*12k*)	0.1622	0.3246	0.0510	6
	O5 (*12k*)	0.4946	-0.0107	0.1474	6
$Sr\ Al_4(Sn_{0.5}Cr_{0.5})_{0.6}Fe_{7.4}O_{19}$	Sr (*2d*)	0.6667	0.3333	0.2500	1
	Fe1(*2a*)	0.0000	0.0000	0.0000	1
	Fe2(*2b*)	0.0000	0.0000	0.2531	1
	Fe3($4f_1$)	0.3333	0.6667	0.0266	2
	Fe4($4f_2$)	0.3333	0.6667	0.1870	1.4
	Sn($4f_2$)	0.3333	0.6667	0.1870	0.3
	Cr($4f_2$)	0.3333	0.6667	0.1870	0.3
	Fe5(*12k*)	0.1640	0.3279	-0.1078	2
	Al(*12k*)	0.1640	0.3279	-0.1078	4
	O 1(*4e*)	0.0000	0.0000	0.2029	2

	O2 (*4f*)	0.3333	0.6667	-0.0811	2
	O3 (*6h*)	0.1640	0.3270	0.25000	3
	O4 (*12k*)	0.1600	0.3190	0.0503	6
	O5 (*12k*)	0.4873	-0.0252	0.1533	6
$Sr\ Al_4(Sn_{0.5}Cr_{0.5})_{0.8}Fe_{7.2}O_{19}$	Sr (*2d*)	0.6667	0.3333	0.2500	1
	Fe1(*2a*)	0.0000	0.0000	0.0000	0.9
	Cr1(*2a*)	0.0000	0.0000	0.0000	0.1
	Fe2(*2b*)	0.0000	0.0000	0.2530	1
	Fe3($4f_1$)	0.3333	0.6667	0.0297	2
	Fe4($4f_2$)	0.3333	0.6667	0.1867	1.4
	Sn($4f_2$)	0.3333	0.6667	0.1867	0.4
	Cr($4f_2$)	0.3333	0.6667	0.1867	0.3
	Fe5(*12k*)	0.1680	0.3360	-0.1072	2
	Al(*12k*)	0.1680	0.3360	-0.1072	4
	O 1(*4e*)	0.0000	0.0000	0.1937	2
	O2 (*4f*)	0.3333	0.6667	-0.0729	2
	O3 (*6h*)	0.1678	0.3356	0.2500	3
	O4 (*12k*)	0.1570	0.3150	0.0529	6
	O5 (*12k*)	0.4960	-0.0070	0.1484	6

From Table 6.2, it is seen that the lattice parameter (LP) '*c*' gradually decreases whereas, '*a*' rests almost constant with increasing 'x'. This decrease in LP ascribes to the effect of doping of smaller ionic radii ion Cr^{+3} (0.52Å) at the place of Fe^{+3} (0.64Å) [Hankare *et al*. (2009), Ashiq *et al*. (2011)]. While, the ionic radii of Sn^{+4} (0.69Å) is larger than Fe^{+3}, it seems that Sn^{+4} doesn't affect the lattice parameters significantly at the smaller concentration. Further increasing the concentration of Sn^{+4}, it affects the LP in the structure significantly. From Table 6.2, it is also observed that the LP increases at x = 0.8. This result

is harmony with the reported literature by Jamalian *et al.* (2014). From Figure 6.2 (b), the XRD profile (220) shifts from 64.31° in x = 0.0 to 64.57° up to x = 0.6 and profile (2014) shifts to higher angle from 68.85° in x = 0.0 to 69.05° up to x = 0.6. While, for x = 0.8, peak shifting is observed towards the lower angle for (220) and (2014) profile. It confirms the increase of LPs and cell volume of synthesized ferrite for x = 0.8 composition.

'*c/a'* ratio is found to be in the range of 3.93-3.83 in all the compositions. This ratio is lower than 3.98, which support the formation of hexaferrite structure [Auwal *et al*. (2016a)]. The crystallite size is measured by the Debye Scherrer's formula [Rasly and Rashad (2013)] (as described in section 3.2.3) with using the Caglioti equation 3.12. It is noted that the crystallite size decreases up to x = 0.6 then, it is increased with Cr-Sn substitutions, as depicted in Table 6.2. Calculated crystallite size is found in the range of 12.64 nm to 11.06 nm. The decrease may be due to smaller ionic radius of the Cr^{+3} ion. It results in lattice shrinkage and decreases in crystallite size. The increase for x = 0.8 composition may be due to the inclusion of larger Sn^{+4} ions into the lattice.

Table 6.4 Grain size, bulk density with EDX analysis of sintered $SrAl_4(Cr_{0.5}Sn_{0.5})_xFe_{8-x}O_{19}$ ferrites with ($0 \leq x \leq 0.8$).

Composition (x)	**Grain Size (µm)**	**Density (g/cm^3)**	**Elemental composition (At%)**				
			Sr	**Al**	**Sn**	**Cr**	**Fe**
0.0	1.11	5.08	3.07	14.09	-	-	34.31
0.2	1.43	5.18	3.96	13.83	0.70	0.18	29.97
0.4	1.67	5.37	3.93	14.05	0.80	0.39	26.85
0.6	1.83	5.56	3.94	12.85	1.39	1.33	24.66
0.8	1.23	5.01	3.86	13.98	1.45	1.64	23.86

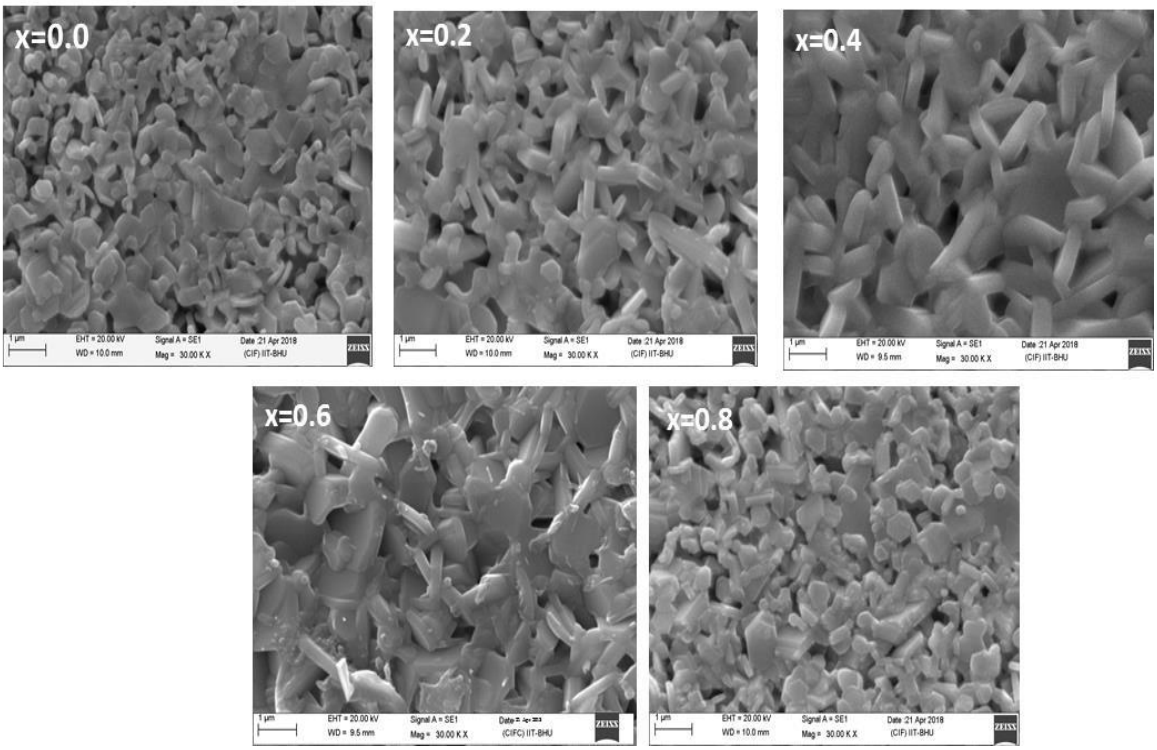

Figure 6.4 SEM micrograph of sintered $SrAl_4Fe_{(8-x)}(Cr_{0.5}Sn_{0.5})_xO_{19}$ ferrites.

Figure 6.4 shows the morphology of sintered $SrAl_4(Cr_{0.5}Sn_{0.5})_xFe_{8-x}O_{19}$ (x = 0.0, 0.2, 0.4, 0.6, & 0.8) ferrite samples. It shows that all the grains are in well-defined hexagonal platelet shape with clear boundaries. Grains are elongated in the *c*-direction, which is obligatory for magnetization of strontium hexaferrite [Kim *et al*. (2016)]. Average grain size is determined by linear intercept through image J software and enlisted in Table 6.4 along with bulk density and EDX elemental analysis. Grain size is increased up to x = 0.6 later, it is decreased with Cr^{+3} and Sn^{+4} content. The similar trend is also found in bulk density. Increasing in grain size may be due to Sn^{+4}, which increases the driving force of sintering, results grain boundary (GB) to move with very fast rate [Rao *et al*. (1999b)]. Further, decreasing in grain size may be due to segregation of doping content at the GB. After limiting substitution of dopant concentration, higher valences induce the micro-voids and

vacancies in the system. Increasing in vacancies or micro-voids due to bulk diffusion of the cations pay to decrease the density as well as grains of the system [Mehar *et al*. (2015)].

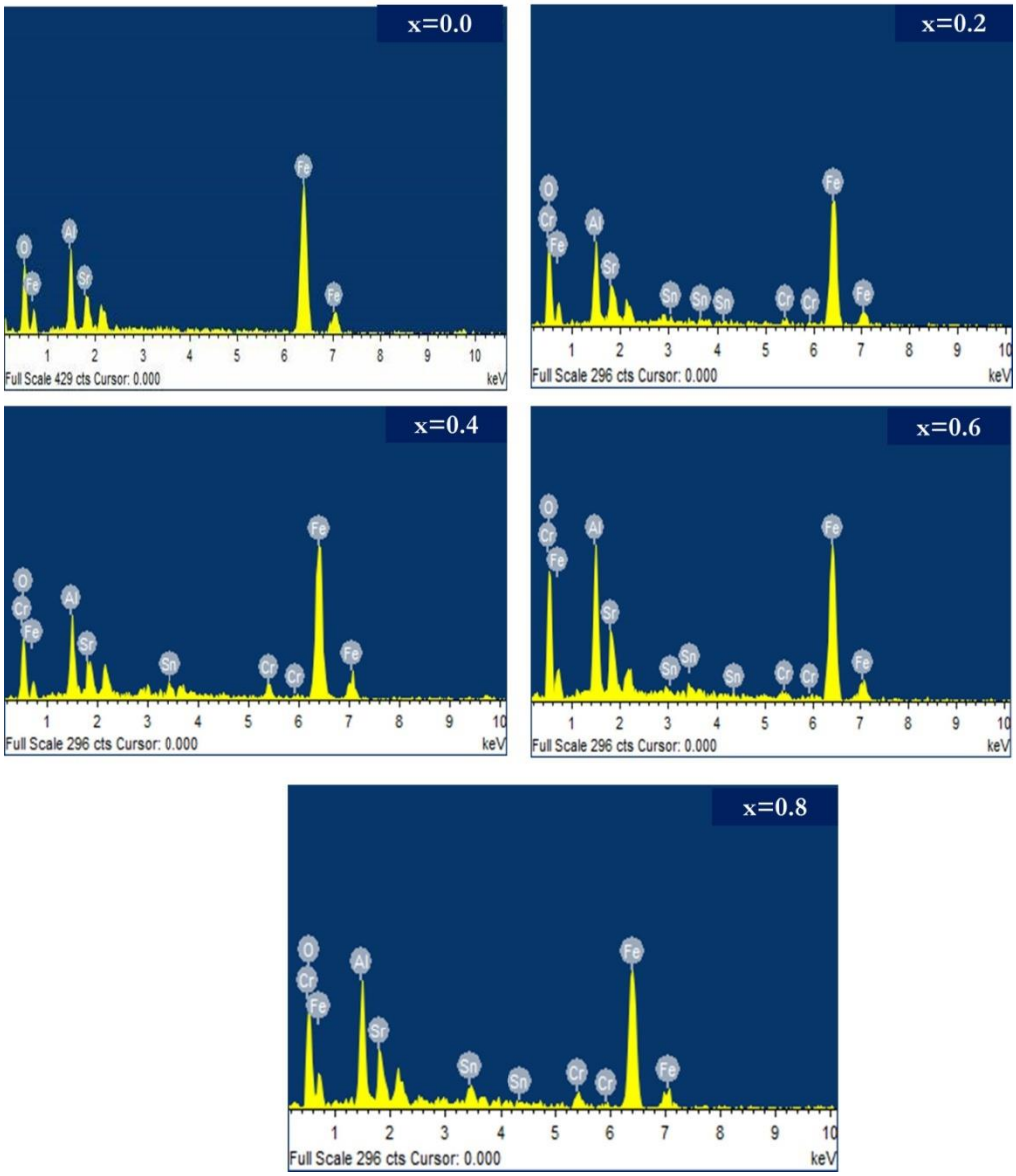

Figure 6.5 EDX micrograph of sintered $SrAl_4Fe_{(8-x)}(Cr_{0.5}Sn_{0.5})_xO_{19}$ ferrites.

EDX elemental analysis is performed to confirm the chemical composition of synthesized $SrAl_4(Cr_{0.5}Sn_{0.5})_xFe_{8-x}O_{19}$ ferrite, as represented in Figure 6.5. Table 6.4 presents the atomic percentage (At %) of Sr, Al, Cr, Sn and Fe in hexaferrites. It shows that At % of

Sn and Cr are increased while, that of Fe^{+3} is decreased with increasing 'x'. Figure 6.6 shows the elemental mapping of selected samples (x = 0.0 & 0.8). It suggests that Sr, Al, Cr, Sn and Fe are distributed homogeneously and no other impurity elements are detected.

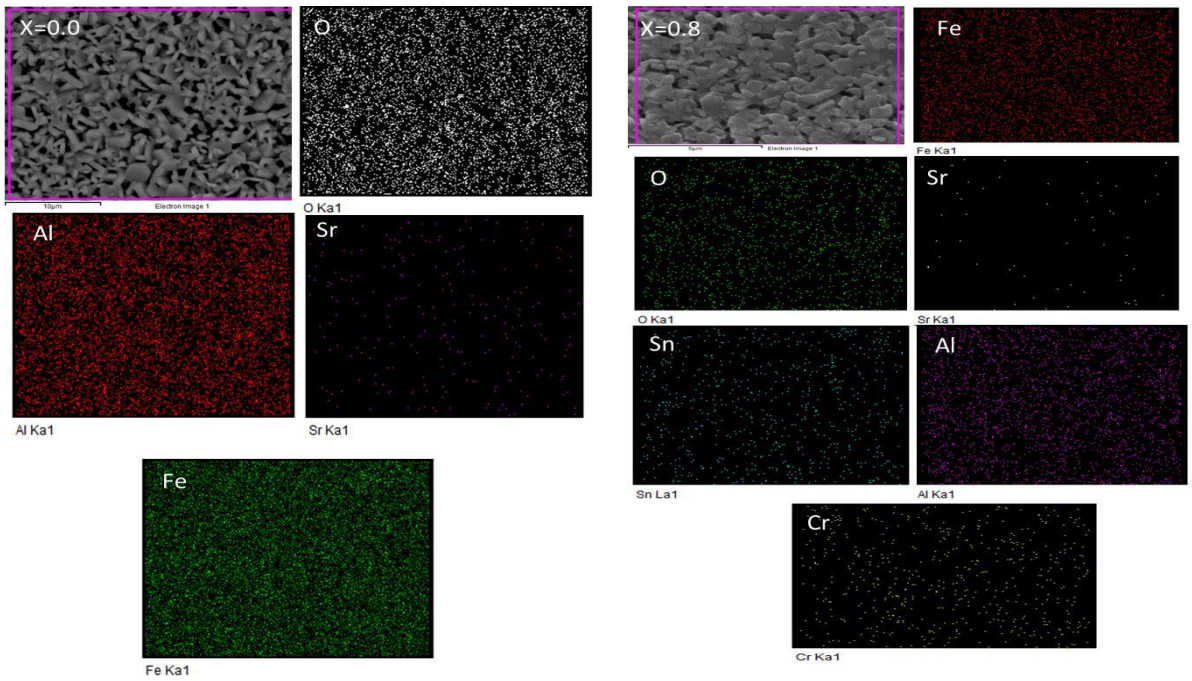

Figure 6.6 Elemental mapping of $SrAl_4Fe_{(8-x)}(Cr_{0.5}Sn_{0.5})_xO_{19}$ ferrites at x = 0.0 and 0.8 composition.

Figure 6.7 to Figure 6.13 reveals the magnetic behavior of Cr-Sn substituted $SrAl_4(Cr_{0.5}Sn_{0.5})_xFe_{8-x}O_{19}$ ($0 \leq x \leq 0.8$) ferrites at room temperature. Figure 6.7 shows the *M–H* loops of $SrAl_4(Cr_{0.5}Sn_{0.5})_xFe_{8-x}O_{19}$ ($0 \leq x \leq 0.8$) ferrites up to an applied field of 7 Tesla. Flux density (*B*), is theoretically calculated by the equation 3.16 from the *M-H* graph. Figure 6.8 shows the variation of theoretically calculated *Br* with a bulk density as a function of Cr-Sn concentration. The values of the magnetic properties are included in Table 6.5. The variation in *Br* is found to increase up to x = 0.6 then, follows a decreasing trend

with increasing the doping content. The remanence *Br* can also be explained as [Huang *et al*. (2017)]:

$$B_r = 4\pi\, M_s\, \rho\, k_{eff} \tag{6.1}$$

Where, *Br* mainly depends on M_s (saturation magnetization), ρ (density) and k_{eff} (magnetic anisotropy). The improvement of *Br* is due to an increase in saturation magnetization and magnetic anisotropy. Magnetic properties are a mixture of extrinsic and intrinsic properties of ferrite. M_s is mainly influenced by the occupation sites of doping cations, magnetic moment and bulk density [Cui *et al*. (2014)]. Magnetic parameters are calculated as described in 3.4.4 section. Figure 6.9 shows the linear fitting between *M* and $1/H^2$ of $SrAl_4Fe_{(8-x)}(Cr_{0.5}Sn_{0.5})_xO_{19}$ ferrites for x = 0.0 and x = 0.8 compositions.

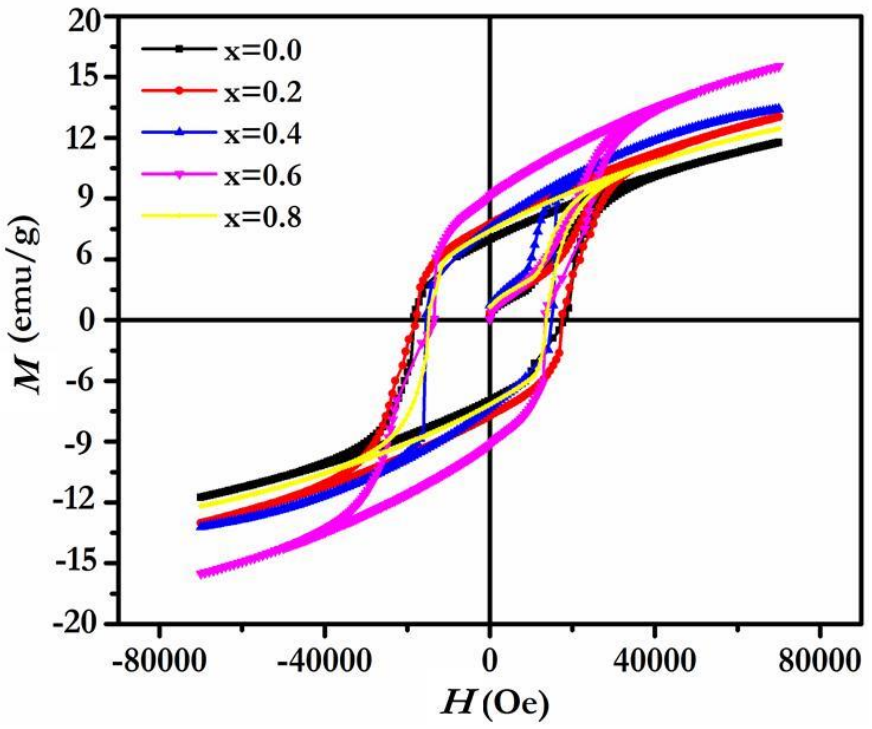

Figure 6.7 Magnetization (*M*) versus field (*H*) at 300K as a function of the Cr & Sn concentration.

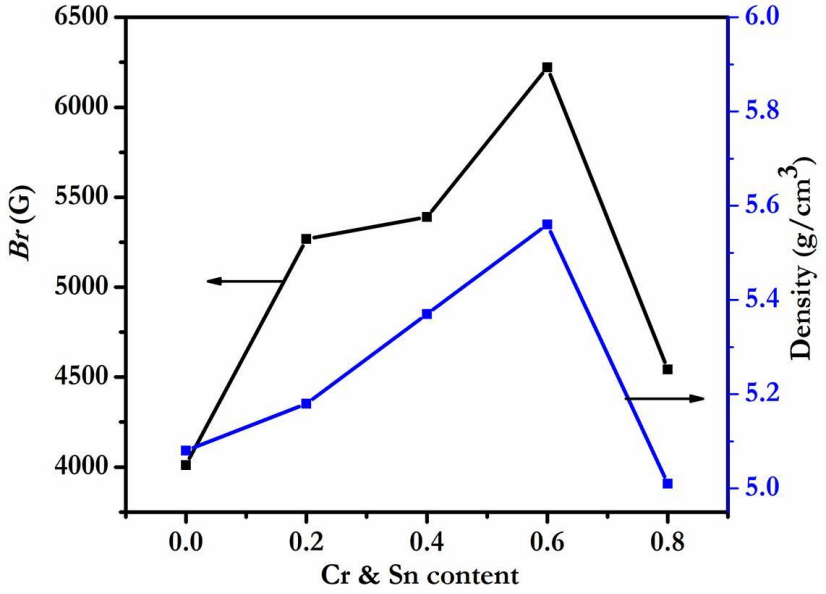

Figure 6.8 *Br* and bulk density as a function of the Cr & Sn concentration.

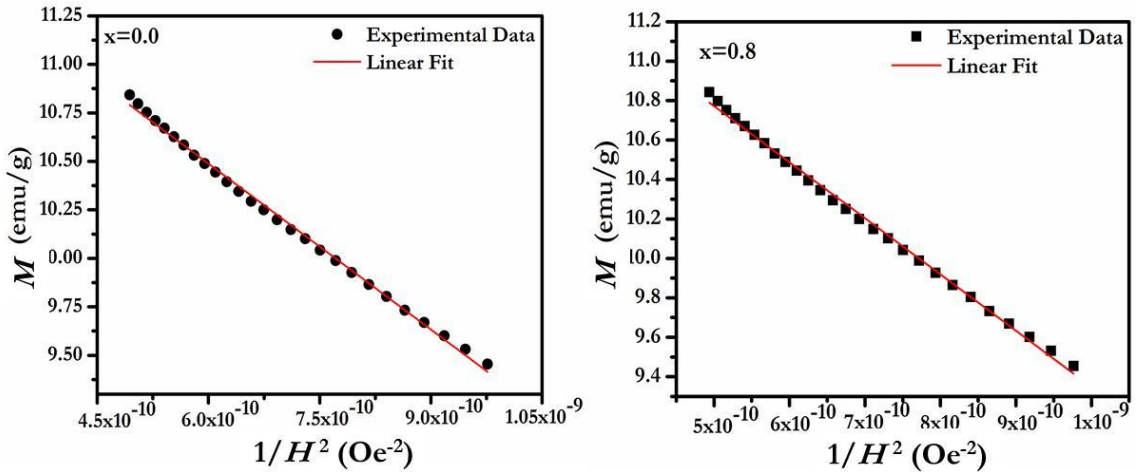

Figure 6.9 Magnetization versus $1/H^2$ plots of $SrAl_4Fe_{(8-x)}(Cr_{0.5}Sn_{0.5})_xO_{19}$ ferrites with x = 0.0 and x = 0.8.

The improvement in M_s can be presumed by two reasons, i.e., bulk density and the occupation preference of the substituted ions. As previously reported, Cr^{+3} occupies either of *12k*, *2a*, and $4f_2$ sites whereas, Sn^{+4} prefers to occupy only $4f_2$ [Jauhar *et al.* (2011), Jamalian

(2015)]. Sakoor *et al*. (2014) have claimed that at the lower concentration of Cr^{+3} prefers $4f_2$ (spin down) site and it increases the magnetization. An increase in M_s up to x = 0.6 indicates that Fe^{+3} is being substituted by Cr^{+3} ion from $4f_2$ (spin down) site. At x = 0.8, the M_s is decreased. This decrease in M_s indicates that the Cr^{+3} ions preferably occupy *2a* (spin up) site (as shown in Table 6.3). It leads to decrease the total magnetic moment ,which reduces the M_s of the system. Non-magnetic Sn^{+4} occupy $4f_2$ site but, it is not affecting the saturation magnetization of the system. The substituted Sn (no unpaired electrons) elements lead to no alter in the unpaired electrons.

Table 6.5 Magnetic parameters *Br*, iH_c, bH_c, H_k/iH_c, $(BH)_{max}$, k_{eff}, and Tc of sintered $SrAl_4(Cr_{0.5}Sn_{0.5})_xFe_{8-x}O_{19}$ ferrites with ($0 \leq x \leq 0.8$).

Composition (x)	***Br*** **(kG)**	***iH*$_c$** **(kOe)**	***bH*$_c$** **(kOe)**	**H_k / *iHc***	**$(BH)_{max}$ (MGOe)**	**$k_{eff\ x10}^{6}$ (erg/cm^3)**	**Tc (ºC)**
0.0	4.10	18.15	18.02	0.89	6.03	3.54	320
0.2	5.26	17.10	16.98	0.89	6.11	4.49	327
0.4	5.38	15.29	15.13	0.90	6.21	4.50	331
0.6	6.22	13.25	13.07	0.91	7.26	5.09	357
0.8	4.54	14.29	14.08	0.88	6.28	4.35	280

Conventionally in metals, all magnetic spins are connected with each other through the direct exchange, but they tend to be neglected with increasing distance between magnetic ions. In the SrM, Fe^{+3} ions are distributed in five different sites, which are coupled magnetically by the super-exchange interaction through O^{-2} ions [Zi *et al.* (2018)]. These interactions can be compared analytically by the structural aspects such as bond lengths and bond angles between the magnetic ions. Anderson *et al.* have suggested that the magnetic

interactions may be strongest if the bond angle, Fe^{+3}_i - O^{-2} - Fe^{+3}_j ($1 \leq i \ \& \ j \leq 5$) is close to 180° and it may be weakest if the bond angle is near to 90° [Anderson *et al.* (1963)]. Additionally, the magnetic interactions may become insignificant over 3Å of bond length [Anderson *et al.* (1963)]. Table 6.6 shows the average Fe-O bond lengths within the sub-lattices of the hexaferrites.

Table 6.6 Average Fe-O bond lengths in $SrAl_4(Cr_{0.5}Sn_{0.5})_xFe_{8-x}O_{19}$ with ($0 \leq x \leq 0.8$)

Site	**Bond Type**	**0.0 Avg.**	**0.2 Avg.**	**0.4 Avg.**	**0.6 Avg.**	**0.8 Avg.**
Fe1 (*2a*, O)	Fe-O	1.931(0)	1.932(0)	1.931(1)	1.929(1)	1.930(0)
Fe2 (*2b*,TBP)	Fe-O	1.793(1)	1.791(0)	1.792(0)	1.790(1)	1.793(0)
Fe3 ($4f_1$,T)	Fe-O	2.031(0)	1.953(1)	1.866(0)	1.854(2)	1.909(1)
Fe4 ($4f_2$,O)	Fe-O	2.086(1)	2.038(0)	2.024(1)	1.934(1)	2.005(0)
Fe5 (*12k*,O)	Fe-O	1.976(0)	1.975(1)	1.972(3)	1.969(0)	1.990(1)

Table 6.7 depicts the bond angles between or within the sub-lattice in the system. All the bond lengths are less than 3 Å, which indicates that the interactions among magnetic ions are significant and contribute an important role in the magnetic properties of the system. Although, it is rather difficult to see the exact effect of bond angles among magnetic interactions. However, it is observed that the bond angles are tending to increase and bond length of $4f_2$ are finding to decrease up to x = 0.6. It indicates the increase in interactions and hence the increase in saturation magnetization, M_s, accordingly. This result is agreed with Das *et al*. (1985). On the other hand, in compositions x = 0.8 the bond angles are tending to decrease meanwhile, bond length of $4f_2$ is finding to increase. It suggests to decrease in interactions and hence a decrease in the saturation magnetization. A schematic diagram is

shown in Figure 6.10 about the nature of bond length of the $4f_2$ site of doped (x = 0.6) and un-doped (x = 0.0) composition.

Table 6.7 Fe^{+3}_i - O^{-2} - Fe^{+3}_j ($1 \leq i \ \& \ j \leq 5$) bond angles for $SrAl_4(Cr_{0.5}Sn_{0.5})_xFe_{8-x}O_{19}$ ($0 \leq x \leq 0.8$).

Bond Type	0.0	0.2	0.4	0.6	0.8
Fe1(*2a*)-O4-Fe3($4f_1$)	126.513(0)	127.701(1)	127.272(0)	128.115(0)	125.910(0)
Fe1(*2a*)-O4-Fe5(*12k*)	92.120(3)	96.780(0)	98.703(2)	101.500(0)	96.325(2)
Fe2(*2b*)-O3-Fe4($4f_2$)	135.321(0)	140.201(1)	142.509(0)	145.101(1)	141.131(0)
Fe2(*2b*)-O1-Fe5(*12k*)	126.517(0)	131.421(0)	134.121(1)	134.222(0)	128.767(1)
Fe3($4f_1$)-O2-Fe5(*12k*)	110.011(4)	116.313(2)	122.360(1)	125.571(1)	115.749(3)
Fe4($4f_2$)-O5-Fe5(*12k*)	127.217(0)	127.676(1)	128.289(0)	130.713(2)	130.579(0)
Fe4($4f_2$)-O3-Fe4($4f_2$)	95.151(0)	98.281(0)	99.901(0)	104.013(0)	92.535(1)
Fe5(*12k*)-O5-Fe5(*12k*)	92.017(1)	100.368(0)	100.501(2)	101.121(4)	94.808(0)
Fe5(*12k*)-O4-Fe3($4f_1$)	114.416(0)	119.918(0)	119.623(3)	123.799(0)	120.518(2)
Fe5(*12k*)-O2-Fe5(*12k*)	94.213(1)	96.391(0)	101.826(0)	102.527(3)	89.681(0)

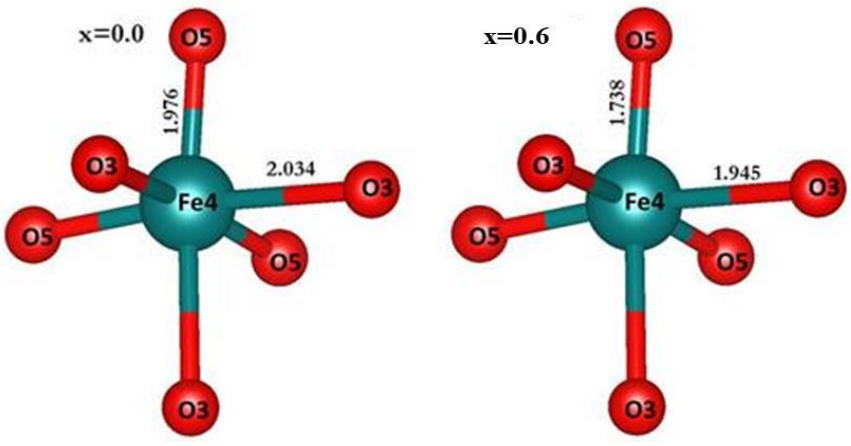

Figure 6.10 Schematic of octahedral site $4f_2$ (Fe4) in $SrFe_8Al_4O_{19}$ (x = 0.0) and $SrAl_4(Cr_{0.5}Sn_{0.5})_{0.6}Fe_{7.4}O_{19}$ (x = 0.6) ferrites.

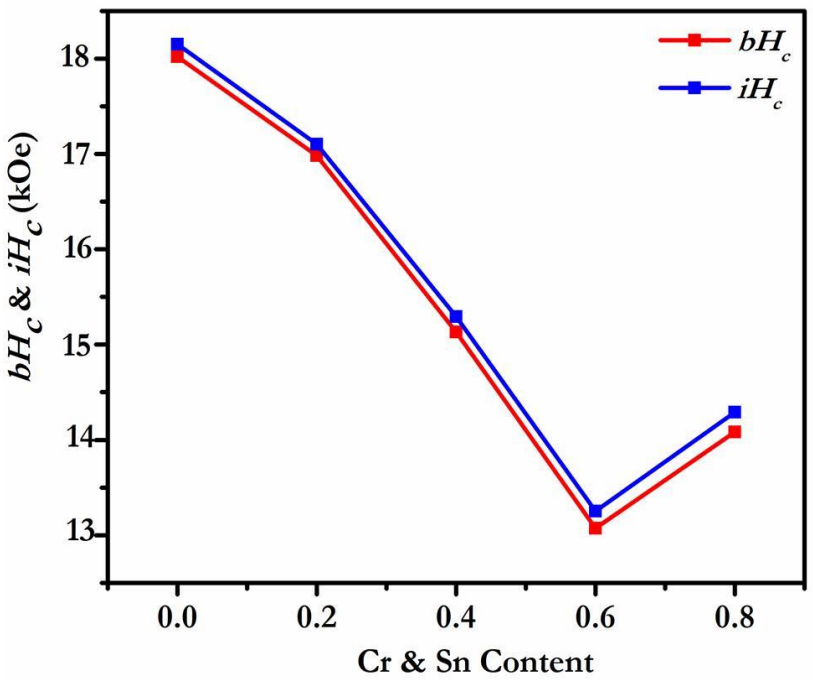

Figure 6.11 Magnetic induction coercivity (bH_c) and intrinsic coercivity (iH_c) as a function of the Cr & Sn concentration.

As shown in Figure 6.11 as well as Table 6.5, coercivity *(iH_c* and *bH_c)* is decreased up to x = 0.6 then increased with substitution. The bH_c is the magnetic induction coercivity, which is induced in the magnetic field due to the allocation of induction (B) to alter their direction. Generally, it is lesser than the intrinsic coercivity (iH_c). Decrease in the H_c mainly due to the increase in grain size [Hooda *et al.* (2015)]. With the increase in grain size, the number of grain boundaries decreases and reduces the domain wall motion, therefore, requires less coercive field (H_c) to relax the system. Figure 6.12 demonstrates the ratio of H_k/iH_c. H_k/iH_c is the so-called squareness ratio, which is the demagnetization curve in the presences of the external magnetic field. The high squarness ratio is required for stable magnetic properties in the permanent magnetic application. This ratio is around 0.89 with Cr-Sn content. Normally, this ratio should be >0.85, for permanent magnetic materials.

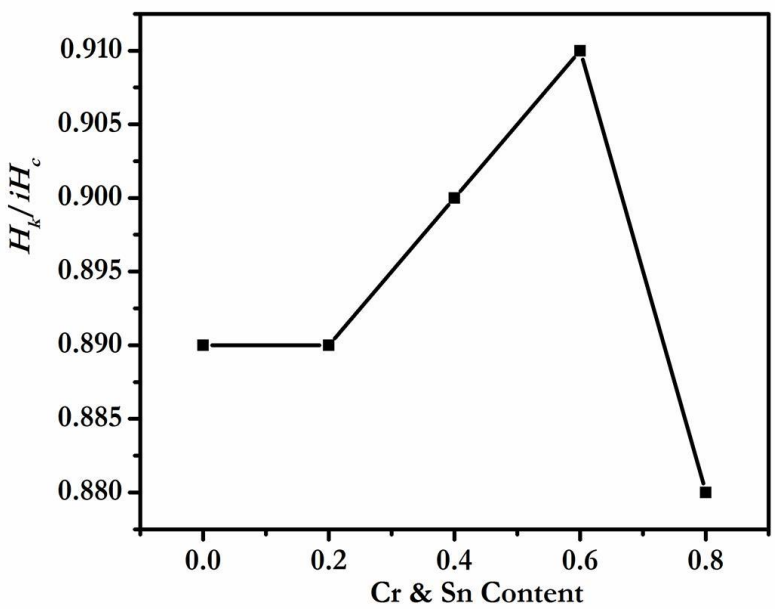

Figure 6.12 H_k/iH_c as a function of the Cr & Sn concentration.

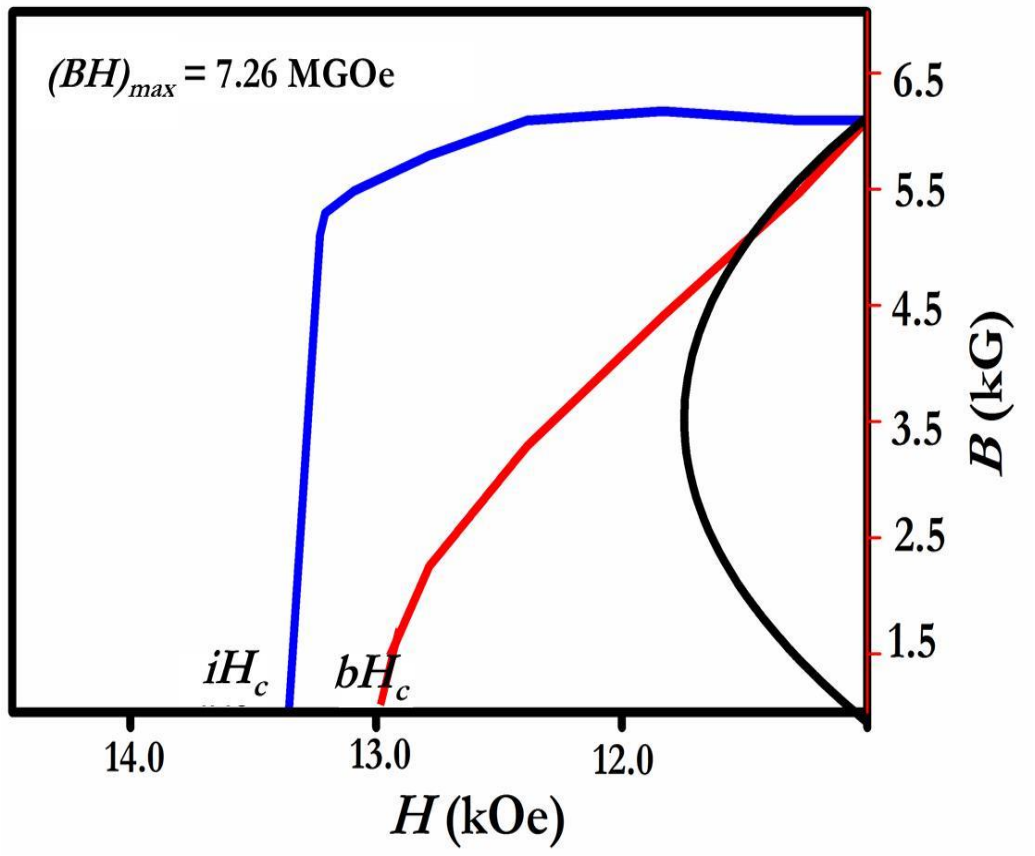

Figure 6.13 Typical demagnetizing curve of the $SrAl_4(Cr_{0.5}Sn_{0.5})_{0.6}Fe_{7.4}O_{19}$ ferrite.

In Table 6.5, it is observed that the theoretically calculated $(BH)_{max}$ is increased up to x = 0.6 further, it is decreased with doping. Figure 6.13 shows the demagnetization curve for x = 0.60 composition. Maximum theoretically calculated $(BH)_{max}$ is 7.26 MGOe, observed at x = 0.6. The value is higher from the earlier reported Cr doped SrM (31.5 kJ/m^3 ~ 3.95 MGOe) [Huang *et al.* (2015)].

From Table 6.5, it is also found that the anisotropy constant, $k_{eff,}$ gradually increases up to x = 0.6 then, decreases with dopant concentrations. This nature of k_{eff} is mainly dependent on the Fe-O-Fe magnetic networks of the 5 different crystallographic sites of Fe^{+3}. Ghimire *et al.* (2018) have reported that each site contributes k_{eff} in the order of *2b*> $4f_2$> *2a*> $4f_1$> *12k*. In the composition up to x = 0.6, improvement of k_{eff} may be due to preferentially occupation of Cr^{+3} and Sn^{+4} at the $4f_2$ site. The *2b* and $4f_2$ sites give the positive contribution in k_{eff} of the system [Yang *et al*. (2002)]. Further, k_{eff} is found to decrease with the substitution at x > 0.6 because of the structural distortions and/or magnetic ordering discontinuity which is induced by the substitution of Cr^{+3} (*2a*) and Sn^{+4} ($4f_2$) in the magnetic network.

The Curie temperature (Tc) is increased up to x = 0.6 later, it is decreased with the substitution, as shown in Table 6.5. Tc is the transition temperature where, ferro/ferri-magnet changes into paramagnetic. In this transition, collinear spins change into non-collinear order. The improvement in Tc is due to the super-exchange interaction. Curie temperature may be expressed with Fe-O-Fe indirect super-exchange interactions [Trukhanov *et al.* (2017a)]. The increase in Curie temperature with substitutions may be because of super-exchange interaction between the Fe ions which is increased, as described earlier. With further substitution creates a divergence of the collinear arrangement of the magnetic moment that is

so-called spin-canting structure [Liu *et al*. (2006)]. The spin-canting structure that is responsible for decreasing of Tc. This result agrees with the earlier reported [Rao *et al.* (1999a)].

Table 6.8 Dielectric constant (Ɛ) and Resistivity (ρ) of sintered $SrAl_4(Cr_{0.5}Sn_{0.5})_xFe_{8-x}O_{19}$ ferrite with ($0 \leq x \leq 0.8$).

Composition (x)	**$\mathcal{E}$ at 1MHz**	**ρ (Ω-cm) x 10^4 at 1MHz**
0.0	20.52	5.54
0.2	23.92	5.23
0.4	25.04	4.53
0.6	32.42	4.49
0.8	28.46	4.97

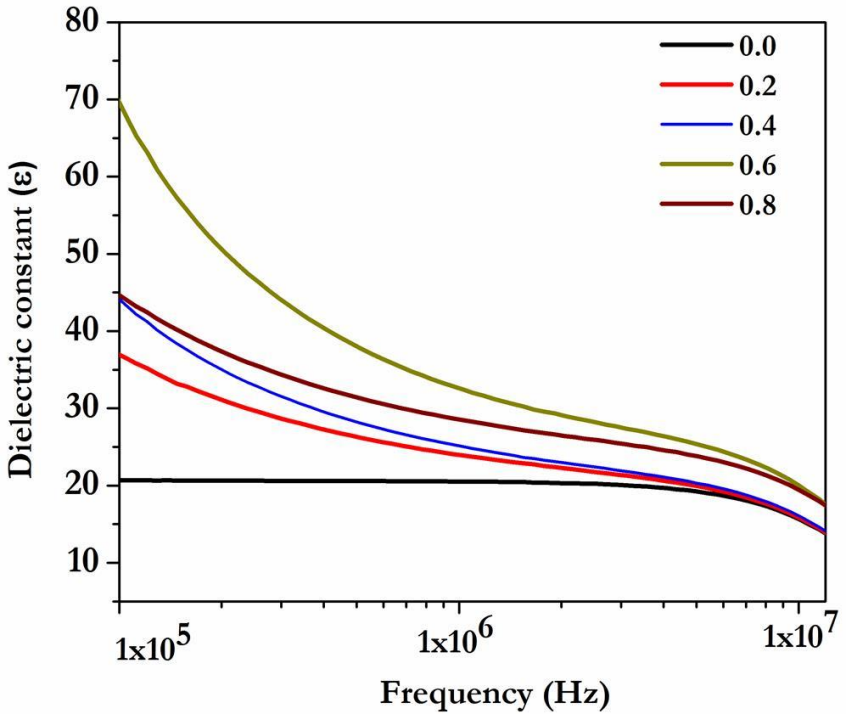

Figure 6.14 Dielectric constant with frequency as a function of the Cr & Sn concentration.

Figure 6.14 shows the dielectric constant (ε) variation with frequency and Table 6.8 summarizes the values at 1MHz. The ε of the synthesized sample is calculated by using equation 3.24. It is clear from Figure 6.14 that dielectric constant is decreased with frequency. According to Iwauchi (1983), the dielectric polarization mechanism is due to electrons hopping in ferrites similar to the conduction mechanism. Large dielectric constant is observed at the lower frequency while, it becomes independent and reduces the value of dielectric constant at higher frequencies. The dielectric structure in ferrites are made up by two layers [Ishaque *et al.* (2016)]. First layer is made up through conducting grains and second layer comprises resistive grain boundaries. It is the reason for the localized accretion of charges under the applied electric field. Resultant some interfacial polarization is occurred between Fe^{+2} and Fe^{+3} ions. At higher frequency filed, electron exchange between Fe^{+2} and Fe^{+3} ions may not follow the external applied field, results in decrease the interfacial polarization contribution and hence, dielectric constant decreases. From Table 6.8, it is found that Ɛ is increased due to the increase in grain size, as shown in Table 6.4. Due to increment in the grain size, ion polarization may be increased with the growth of grain necking. The polarization of ions greatly affects the dielectric constant [Hassan *et al.* (2014)]. When the grain size is increased, it decreases the grain boundary concentration among them. As a result, it reduces the limitation in the motion of the domain wall, which improves the dielectric constant.

Figure 6.15 shows the variation of AC resistivity (ρ) with frequency. All samples show a decrease in ρ with the increase in frequency. The electric resistivity of $SrAl_4(Cr_{0.5}Sn_{0.5})_xFe_{8-x}O_{19}$ are investigated and Table 6.8 shows the variation of electric resistivity with the function of Cr^{+3} and Sn^{+4}. The resistivity gradually decreases with

substitution up to x = 0.6, later it is increased. Nature of resistivity can be defined due to grain size. As listed in Table 6.4, the grain size is increased with the substitution up to x = 0.6. Increasing in grain size reduces the grain boundary. Grain boundary creates the hindrance in the system. Henceforth with substitution, resistivity is decreased up to x = 0.6 due to decrement in the GB. Further, with substitution at x = 0.8, it reduces the grain size and enhances the grain boundary (GB) area. Grain boundary obstructs the electron transfer, therefore, increases in resistivity at x = 0.8.

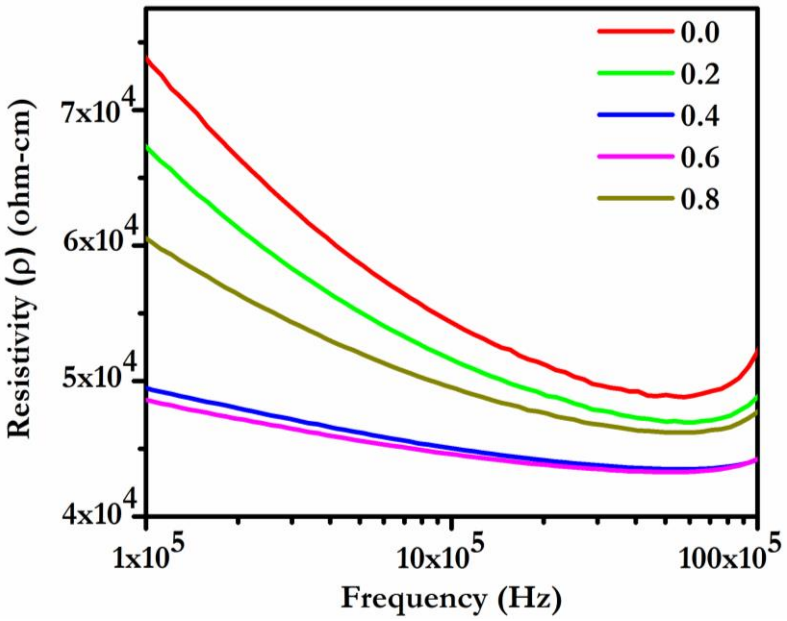

Figure 6.15 Resistivity with frequency as a function of Cr & Sn concentration.

6.3 Summary

Cr^{+3} and Sn^{+4} substituted strontium hexaferrites $SrAl_4(Cr_{0.5}Sn_{0.5})_xFe_{8-x}O_{19}$ with x = 0.0, 0.2, 0.4, 0.6, & 0.8 are successfully synthesized by using the sol-gel auto combustion method. The Rietveld refinement reveals the formation of a hexagonal structure with *P63/mmc* space group with no secondary phase formation. The unit cell parameters, atomic

positions, bond lengths, bond angles are estimated through X-ray diffraction studies. The morphological studies reveal that the average grain size decreases with the dopant concentrations and dopants are homogeneously distributed. The effect of doping on crystal structure, magnetic properties and super-exchange interaction is investigated. The anisotropy constant for all the compositions is calculated. It is observed that the maximum remnant magnetization *Br*, iH_c and $(BH)_{max}$ is found about 6.22 kOe, 13.84 kOe and 7.26 MGOe, respectively at x = 0.6 composition. The improved magnetic properties of the samples may be suitable as a promising candidates for permanent magnets applications.